Control of the Parallel Operation of VSC-HVDC Links Connected to an Offshore Wind Farm

José Luis Rodríguez-Amenedo, *Member, IEEE*, Santiago Arnaltes-Gómez, *Member, IEEE*,
Mònica Aragüés-Peñalba, *Member, IEEE*, Oriol Gomis-Bellmunt, *Senior Member, IEEE*

Abstract—This paper introduces the control of the parallel operation of two VSC-HVDC links interconnecting an offshore wind farm. The aim of the study is to propose and validate a control system that allows the parallel operation of two VSC-HVDC links by controlling the currents injected by the VSC converters. The currents set points are established by a voltage controller in order to maintain constant voltage and frequency in the capacitor of the output filter and therefore within the offshore wind farm (OWF). It is demonstrated that the decoupled control of the d-q component of the voltage at the capacitor allows achieving the direct control of voltage and frequency, respectively. The voltage and frequency control (VFC) is implemented by orienting the capacitor voltage toward a synchronous axis that is generated within the controller and therefore is not subjected to any grid disturbance. Both converters collaborate therefore in maintaining constant voltage and frequency, achieving in this way the parallel operation of the converters. The validation of this approach is demonstrated by simulation where the OWF and the VSC-HVDC rectifier have been modeled. Simulation results demonstrate that the proposed control system allows the parallelization of the converters while maintaining constant voltage and frequency within the OWF, even during transient faults.

Keywords—HVDC, wind power plants, fault ride through

I. INTRODUCTION

Offshore wind farms present a number of benefits compared to traditional onshore wind farms. Amongst the most relevant, the following can be highlighted: the availability of higher wind speed, the ease of transporting of very large structures (allowing larger wind turbines) and the limited available inland locations to install new wind farms in some countries (mainly in Europe). Offshore generation facilities can be connected to the main 50 or 60 Hz AC grid using transmission systems based on High Voltage Alternating current (HVAC) or High Voltage Direct Current (HVDC) [1, 2]. The choice between these technologies depends on the cost of the installation, which depends in turn on the transmission distance and power rating. The proliferation of Offshore Wind Farms (OWFs) is promoting the development of HVDC systems more complex in terms of operation and control. The existing ones are based on simple point-to-point connections, but the natural evolution is to meshed topologies to further enhance the reliability and economical operation of HVDC grids [3]. Likewise, VSC-HVDC stations are evolving to more reliable and flexible configurations.

VSC-HVDC stations connected to OWFs should provide voltage and frequency control on the AC offshore network [4, 5]. Typically, only a single converter is used to connect the AC grid to the HVDC link using a symmetrical monopole

configuration [6]. In the case of connecting new power plants in the area of existing wind farms, two options can be considered. The first one is to construct a new AC/DC substation with an independent DC link, interconnecting both VSCs through an AC line [7]. The second option consists of connecting in parallel these two VSCs to a common AC bus as an extension of the existing substation. This configuration works effectively as two independent point-to-point VSC-HVDC links, enhancing the system reliability [6]. Each VSC can operate at different active power level and they can also be connected to different buses of the main AC grid, increasing the reliability.

Such VSC configurations present some technical challenges regarding voltage and frequency control, active and reactive power sharing and fault ride-through for faults in the offshore AC grid [8]. The main problem is the need to coordinate a plurality of power converters which are imposing the voltage and the angle of the offshore grid. Several researchers have been investigating this problem for offshore grids with only one VSC-HVDC rectifier [9], arriving to the conclusion that careful analysis is needed and that the overall control structure needs to be simplified to prevent system resonances and oscillations. This problem has actually been experienced in some real projects in the North Sea. This issue in systems comprising several VSC-HVDC rectifiers can be theoretically addressed without relying on communications, using Conventional Droop Control (CDC) laws [10], synchronous generator emulation or virtual synchronous machines (VSM) [11, 12, 13] and power synchronization control [14]. While a non-communications solution has undoubtable academic interest, and it can be certainly used whenever a communication failure occurs, the use of fast communication systems can provide enhanced performance and faster dynamic response. If the system with a single VSC-HVDC rectifier is likely to experience resonances, this risk is substantially increased if more rectifiers are added, together with additional distributed control loops. Therefore, the present paper suggests a centralized control approach, using communication systems which will be already existing in the system. Whenever the two VSC-HVDC converter stations are installed in the same or neighboring physical platforms, the option of integrating the controllers and perform a centralized control has several advantages. An integrated and direct control will be simpler than the alternative options using distributed communication-less controllers. The application of the proposed concept will minimize the risk of overall system unstability, which is very important when distributed controllers are used. In fact, stability is one of advantages of the proposed control system over conventional droop control, even more in the case of two converters with different ratings. Basically, the fact that there

is only one central voltage controller, guarantees the stability of the voltage and frequency independently of the converter data. Furthermore, as the converters are connected to two different DC buses, homopolar currents cannot circulate.

This paper presents a direct control of a double VSC HVDC link connected to the same offshore AC collection grid. Unlike distributed control methods, this direct control uses only a centralized voltage and frequency controller. Current references are sent to each VSC, which are automatically parallelized through their own current control loop, while sharing active and reactive power between different converters. In the direct control, slow power controllers are eliminated which allows reducing bandwidths of voltage and current controllers and therefore make possible the use low frequency switching strategies without compromising the stable operation of the system.

The paper is organized as follows. A system description of the OWF connected to the double VSC-HVDC link is shown in Section II. In Section III a systematic approach to the VSCs modeling is presented. In this section the inner control-loops (voltage and current controllers) and the outer power controllers have been integrated in the model. Besides, its state equations have been obtained in a common reference frame. Section IV presents the fundamentals for the direct control of a double VSC station. In Section V the system stability is studied by analyzing the eigenvalues for different parameters. To evaluate the performance of the direct control, time-domain simulation studies in PSIM software are presented in Section VI.

II. SYSTEM DESCRIPTION

Figure 1 shows the transmission system of an OWF connected to the main AC-grid at two different buses through two independent HVDC links. The rectifier station of the OWF comprises two VSCs connected to a common offshore grid bus. The common bus collects the power generated by the OWF and transmitted through AC export cables from the OWF substation. This configuration is known as multi-infeed connection [9]. One of the advantages of this topology is that the wind farm can be enlarged without limiting its rated capacity to the rating of a single HVDC connection. On the other hand, it leads to a more reliable connection as it can keep the offshore wind power transmission to the main grid even if one of the HVDC links fails. Furthermore, it allows a staged progress of the DC connection by different developers [9, 15]. Both VSCs rectifiers are interconnected in the common bus with their corresponding output high-frequency filters, used for the implementation of the proposed voltage and frequency control scheme. The electrical data of the system components is detailed in Section VII.

For simulation purposes the offshore wind farm is modelled as a PQ bus, where the active power is just a function of the wind velocity driving the turbines and the reactive power is the result of load flow with the reactive power adjusted in each wind turbine [16, 17].

III. PARALLEL VSC STATION MODEL

The AC-side of VSCs can be generally represented by a three-phase AC voltage source connected to the system through an interfacing reactor modeled by an inductance
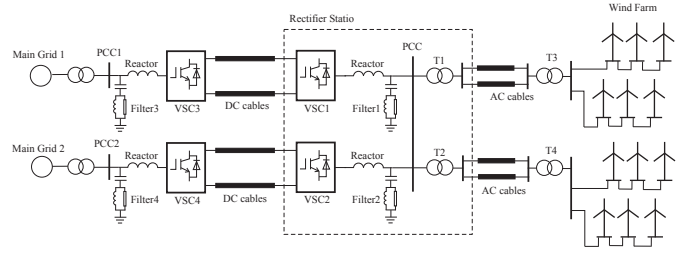

Figure 1: Multi-infeed VSC-HVDC connection of an offshore wind farm

L and a resistance R [18, 19, 20]. In case of modular multilevel converters (MMC) L and R are half of inductance and resistance of the arm reactor [21]. The total capacitance connected at PCC (Point of Common Coupling) is represented by C, which comprises the capacitance of both high frequency filters, which are considered purely capacitive at the fundamental frequency [22] (see Figure 2).

Hierarchical control systems on MMC can be classified into two levels: upper level (voltage and power control) and lower level (submodule and arm control) [23, 24]. In this paper only upper level control is investigated, low level controllers such as balancing capacitor algorithm (BCA), second-harmonic circulating current suppression controller (CCSC) and nearest level modulation (NLM) [25, 26, 27] are assumed to be correctly implemented. Additionally, the modelling of the MMC in the DQ reference includes a variable series capacitor, C_{MMC}, that depends on the modulation index [28].

The DC-side of VSCs is represented by a core-screen coupled π model for a pair of DC cables [29, 30] as shown in Figure 3. The inverter station is operated in constant DC voltage mode to allow the transmission of power from the rectifier station.
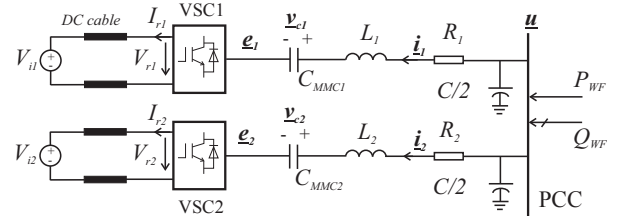

Figure 2: Model of the parallel VSC station

According to Figure 2, the AC-side dynamic equations of currents $\underline{i_k}$ and voltages on the series capacitors $\underline{v_{ck}}$, expressed in a synchronous DQ reference frame rotating at constant frequency ω_0, are:

$$\underline{u} = L_k \frac{d\underline{i_k}}{dt} + j\omega_0 L_k \underline{i_k} + R_k \underline{i_k} + \underline{v_{ck}} + \underline{e_k} \qquad (1)$$

$$\underline{i_k} = C_{MMC_k} \frac{d\underline{v_{ck}}}{dt} + j\omega_0 C_{MMC_k} \underline{v_{ck}} \qquad (2)$$

being the subscript k the converter number, $k = 1, 2$. Likewise, the dynamic equation of the voltage on AC capacitor connected at PCC is represented as:

$$\underline{i_{WF}} - (\underline{i_1} + \underline{i_2}) = C \frac{d\underline{u}}{dt} + j\omega_0 C \underline{u} \qquad (3)$$

where the current vectors of each VSC and the wind farm are, $\underline{i_k} = i_{kD} + ji_{kQ}$ and $\underline{i_{WF}} = i_{WFD} + ji_{WFQ}$,

respectively. The voltage vector at the PCC bus is represented as $\underline{u} = u_D + ju_Q$ and the internal voltages of each VSC as $\underline{e_k} = e_{kD} + je_{kQ}$

The internal voltages e_{kD} and e_{kQ} are obtained as a result of the control action depending on the DC voltages V_{kr}, according to [31]:

$$e_{kD} = \frac{1}{2}m_{kD}V_{kr} \qquad e_{kQ} = \frac{1}{2}m_{kQ}V_{kr} \qquad (4)$$

where m_{kD} and m_{kQ} are the DQ modulation indexes obtained by the Park transformation of the phase modulation signals of each VSC. Likewise, the series capacitor C_{MMC} can be expressed as a function of these modulation indexes [32] as

$$C_{MMC_k} = \frac{64C_{arm}}{8 - 3(m_{kD}^2 + m_{kQ}^2)} \qquad (5)$$

In Equation (5) the capacitance of each arm C_{arm} is calculated as the equivalent capacitor of n-numbers of cells connected in series on each arm [33]. By taking real and imaginary parts, (1)-(3), and rearranging terms, the derivatives of the state variables at the AC-side are expressed as:

$$L_k\frac{di_{kD}}{dt} = -R_k i_{kD} + \omega_0 L_k i_{kQ} + u_D - v_{ckD} - \frac{1}{2}m_{kD}V_{kr} \quad (6)$$

$$L_k\frac{di_{kQ}}{dt} = -R_k i_{kQ} - \omega_0 L_k i_{kD} + u_Q - v_{ckQ} - \frac{1}{2}m_{kQ}V_{kr} \quad (7)$$

$$C_{MMC_k}\frac{dv_{ckD}}{dt} = i_{kD} + \omega_0 C_{MMC_k} v_{ckQ} \qquad (8)$$

$$C_{MMC_k}\frac{dv_{ckQ}}{dt} = i_{kQ} - \omega_0 C_{MMC_k} v_{ckD} \qquad (9)$$

$$C\frac{du_D}{dt} = \omega_0 C u_Q + i_{WFD} - (i_{1D} + i_{2D}) \qquad (10)$$

$$C\frac{du_Q}{dt} = -\omega_0 C u_D + i_{WFQ} - (i_{1Q} + i_{2Q}) \qquad (11)$$

where currents i_{WFD} and i_{WFQ} can be expressed in terms of: a) external inputs P_{WF} and Q_{WF} and b) DQ-components of voltage at the common bus u_D and u_Q

$$i_{WFD} = \frac{2}{3}\frac{P_{WF}u_D + Q_{WF}u_Q}{u_D^2 + u_Q^2} \qquad (12)$$

$$i_{WFQ} = \frac{2}{3}\frac{P_{WF}u_Q - Q_{WF}u_D}{u_D^2 + u_Q^2} \qquad (13)$$

Assuming that the power transmitted from the internal voltages is equal to the DC power of the rectifier

$$V_{kr}I_{kr} = \frac{3}{2}(e_{kD}i_{kD} + e_{kQ}i_{kQ}) \qquad (14)$$

the DC current of each VSC rectifier I_{kr} can be calculated in terms of m_{kD} and m_{kQ} as

$$I_{kr} = \frac{3}{4}(m_{kD}i_{kD} + m_{kQ}i_{kQ}) \qquad (15)$$

On the other hand, Figure 3 shows the core-screen coupled π model for a single DC cable. The state variables of this model are the DC voltage of the rectifier, V_{kr}, the core current, I_{kco}, and the screen current, I_{ksc}.
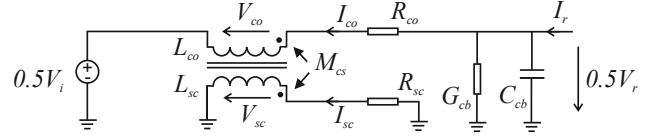

Figure 3: DC cable model

Applying the first Kirchoff law, the voltage rectifier dynamics is obtained as:

$$C_{kcb}\frac{dV_{kr}}{dt} = 2(I_{kr} - I_{kco}) - G_{kcb}V_{kr} \qquad (16)$$

being C_{kcb} and G_{kcb} the parallel capacitance and conductance of each cable, respectively. The state equations of the DC coupled inductance are represented as:

$$V_{kco} = L_{lco}\frac{dI_{kco}}{dt} + M_{kcs}\frac{dI_{ksc}}{dt} = 0.5(V_{kr} - V_{ki}) - R_{kco}I_{kco} \qquad (17)$$

$$V_{ksc} = M_{kcs}\frac{dI_{kco}}{dt} + L_{ksc}\frac{dI_{ksc}}{dt} = -R_{ksc}I_{ksc} \qquad (18)$$

From Equations (17) and (18), the currents' derivatives of core and screen can be obtained as follows:

$$L_{kcs}\frac{dI_{kco}}{dt} = L_{ksc}V_{kco} - M_{kcs}V_{ksc} \qquad (19)$$

$$L_{kcs}\frac{dI_{ksc}}{dt} = -M_{kcs}V_{kco} + L_{kc0}V_{ksc} \qquad (20)$$

where $L_{kcs} = L_{kco}L_{ksc} - M_{kcs}^2$.
Replacing the expressions of V_{kco} and V_{ksc} on Equations (19) and (20), the derivatives of the DC currents can be expressed in terms of the rectifier current I_{kr} and the DC voltage of the inverter V_{ki} as:

$$L_{kcs}\frac{dI_{kco}}{dt} = L_{ksc}(\frac{1}{2}V_{kr} - \frac{1}{2}V_{ki} - R_{kco}I_{kco}) + M_{kcs}R_{ksc}I_{ksc} \qquad (21)$$

$$L_{kcs}\frac{dI_{ksc}}{dt} = -M_{kcs}(\frac{1}{2}V_{kr} - \frac{1}{2}V_{ki} - R_{kco}I_{kco}) - L_{kc0}R_{ksc}I_{ksc} \qquad (22)$$

By linearizing the system, the state space model is obtained, which has sixteen state variables: $\Delta\mathbf{x} = [\Delta u_D, \Delta u_Q, \Delta i_{kD}, \Delta i_{kQ}, \Delta v_{ckD}, \Delta v_{ckQ}, \Delta V_{kr}, \Delta I_{kco}, \Delta I_{ksc}]^T$, two external inputs $[\Delta P_{WFD}, \Delta Q_{WFQ}]^T$ and four control variables, two for each VSC $[\Delta m_{kD}, \Delta m_{kQ}]^T$.

IV. VOLTAGE AND FREQUENCY CONTROL

The objective of the control system is to maintain constant voltage and frequency within the AC grid of the OWF by the parallel operation of the VSC converters. For such purpose, the capacitance of the high frequency filters is used. It is demonstrated that the control of the D-Q axis components of the capacitor voltage will lead to the voltage and frequency control of the AC grid, which in turn is achieved by controlling the active and reactive current flowing into the capacitor [34, 35].

The VFC is based on the orientation of the voltage vector at the capacitor terminals along a synchronous reference axis (D axis), according to Figure 4. The rotational speed of the synchronous reference axis is the reference frequency of the system, i.e. 50 Hz. As long as the control is able to maintain the voltage vector orientated along the synchronous

reference axis, the frequency is kept constant. By controlling the magnitude of the voltage vector, the voltage magnitude is also kept constant. The capacitor voltage vector Equations (10)-(11) are used to derive the control strategy for the voltage and frequency control.
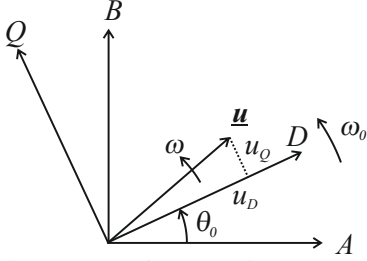

Figure 4: Voltage vector in a synchronous reference frame

In steady state, the capacitor voltage vector is aligned along the synchronous reference axis and therefore $u_D = |\underline{u}|$ and $u_Q = 0$. Therefore, Equation (10) indicates that by keeping constant voltage across the capacitor, the OWF active current is equal to the VSCs active current, as $u_Q = 0$, while Equation (11) stands that the OWF reactive current is equal to the VSCs reactive current plus the capacitor current ($\omega_0 C u_D$).
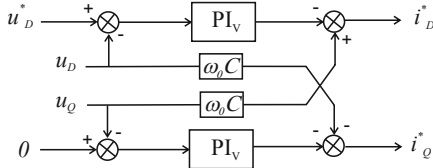

Figure 5: Voltage and frequency control scheme

In conclusion, by keeping constant voltage across the capacitor and keeping the terminal voltage vector aligned along the synchronous reference axis, instantaneous active and reactive power balance between the OWF and the VSCs is achieved. With such principles, the control system is quite simple: there are two control channels. The first one to obtain constant voltage ($u_D = |\underline{u}|$) and the second one to obtain constant frequency ($u_Q = 0$).

In Figure 5, the reference voltage is compared to the D-axis component of the actual voltage vector while the Q-axis component of the actual voltage vector is compared to zero. The reference D-axis orientation is obtained by integration of the desired frequency ω_0, as shown in Figure 7. It should be noted that in Figure 5 the cross-coupling terms of Equations (10) and (11) have been compensated to enhance the dynamics of the control system. From the previous principles, the control of the magnitude and angle of the voltage vector are related to the control of the active and reactive power balance, respectively.

Moreover, the power balancing control has to be achieved by the VSCs active and reactive power control, as the OWF active power is a function of the wind velocity, and therefore can not be used in the proposed control scheme. Therefore, in Equations (10) and (11) the control of the voltage DQ-components is achieved through the control of the active and reactive current drawn by the VSC rectifiers, respectively.

With these relationships, in the control scheme of Figure 5, the control of the voltage magnitude is carried out by the D-component of the rectifiers current vector i_D, while the control of the frequency is carried out by the Q-component of the current vector i_Q. An increment of the rectifiers active current will produce an increment in the capacitor voltage while an increment of the rectifiers reactive current will produce a (negative) increment of the voltage vector rotational speed, that can be used to keep it aligned towards the reference axis. On the other hand, the current control of the VSC converters is well-established in the literature and it is based on the decoupled DQ control through the VSC internal voltage DQ components, respectively (Figure 6). In Figure 6, in order to improve the dynamic response of the current control loop, the cross-coupling terms of Equations (33) and (34) have been compensated, as well as the grid voltage and the voltage drop in the equivalent MMC capacitor. To improve the dynamics of the system this voltage drop is affected by the damping factor k_ζ as will be explained in the following section.
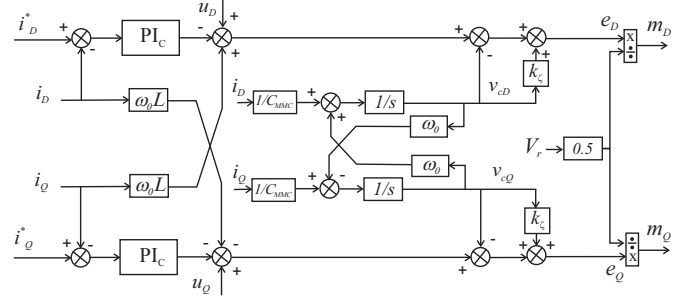

Figure 6: Inner current control loop scheme

With the aforementioned control system, there is only one voltage and frequency controller and both converters are automatically parallelized through the current control loops, i.e, both converters operate synchronously without employing the well-known droop control technique. Moreover, both converters participate on maintaining constant voltage and frequency within the offshore grid. The participation factors can be adjusted independently, if needed, by adding some weights to the current reference of each converter. These participation factors would establish what percentage of the total current has to be supplied by each converter. The participation factors allow a very flexible operation of the VSCs. If one of the VSC participation factors is zero it means that it is not participating in the voltage control, while the other is assuming the whole voltage control (participation factor equals one). Moreover, the VSC not participating in the voltage control, can then have an independent control reference for active and/or reactive power. Finally, Figure 7 shows a schematic representation of the overall control system. Note that a phase-locked loop (PLL) is not needed, because the whole control is oriented to a synchronous axis obtained directly from integration of the desired angular frequency and therefore the angular position is not subjected to any measurement noise or grid disturbance.

V. CONTROLLED SYSTEM STABILITY ANALYSIS

In this section the complete state space model of the double VSC station will be derived from equations obtained in
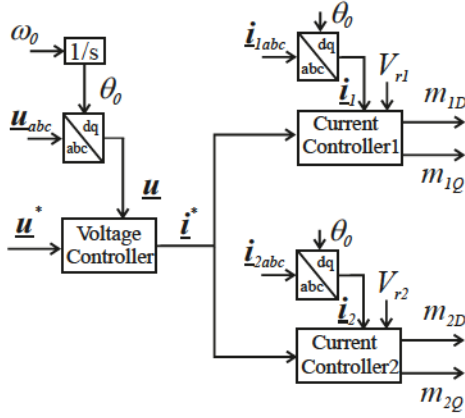
Figure 7: Overall control system scheme

Section III by adding the dynamic equations of the proposed voltage and current proportional+integral controllers, PI_V and PI_C, in Figures 5 and Figure 6, respectively. In the current controllers PI_C the internal voltage of each VSC converter is obtained by the expression:

$$\underline{e_k} = \underline{u} - j\omega_0 L_k \underline{i_k} - \underline{v_{ck}}(1+k_\zeta) - k_C(\underline{i_k^*} - \underline{i}) - \frac{k_C}{T_C}\int(\underline{i_k^*} - \underline{i})dt \quad (23)$$

where k_C and T_C are the current controller proportional gain and integral time constant, respectively, and the compensating terms have been added. Likewise the damping factor k_ζ has also been considered in order to avoid low frequencies oscillations produced by the dynamics of the series capacitors expressed by Equations (8) and (9). By separating into real and imaginary parts and using the modulation indexes definitions from Equation (4):

$$m_{kD} = \frac{2}{V_{kr}}(u_D + \omega_0 L_k i_{kQ} \quad v_{ckD}(1+k_\zeta) \quad k_C(i_{kD}^* \quad i_{kD}) \quad k_C\gamma_{kD}) \quad (24)$$

$$m_{kQ} = \frac{2}{V_{kr}}(u_Q \quad \omega_0 L_k i_{kD} \quad v_{ckQ}(1+k_\zeta) \quad k_C(i_{kQ}^* \quad i_{kQ}) \quad k_C\gamma_{kQ}) \quad (25)$$

where the new state variables are γ_{kD} and γ_{kQ} given by:

$$T_C\frac{d\gamma_{kD}}{dt} = i_{kD}^* - i_{kD} \quad T_C\frac{d\gamma_{kQ}}{dt} = i_{kQ}^* - i_{kQ} \quad (26)$$

Similarly, the voltage controller PI_V input is the voltage error, while the output is the current reference given by:

$$\underline{i_k^*} = j\omega_0 C\underline{u} - k_V(\underline{u^*} - \underline{u}) - \frac{k_V}{T_V}\int(\underline{u^*} - \underline{u})dt \quad (27)$$

where k_v and T_v are the voltage controller proportional gain and integral time constant, respectively, and the compensating cross terms have been added. By separating into real and imaginary parts:

$$i_{kD}^* = \omega_0 C u_Q - k_V(u_D^* - u_D) - k_V\phi_D \quad (28)$$

$$i_{kQ}^* = -\omega_0 C u_D - k_V(u_Q^* - u_Q) - k_V\phi_Q \quad (29)$$

where the new state variables are ϕ_D and ϕ_Q given by:

$$T_V\frac{d\phi_D}{dt} = u_D^* - u_D \quad T_V\frac{d\phi_Q}{dt} = u_Q^* - u_Q \quad (30)$$

On the other hand, the compensation of the voltage drop in MMC equivalent capacitor leads to the following dynamic equations:

$$v_{ckD} = \int(\frac{i_{kD}}{C_{MMCk}} + \omega_0 v_{ckQ})dt \quad (31)$$

$$v_{ckQ} = \int(\frac{i_{kQ}}{C_{MMCk}} - \omega_0 v_{ckD})dt \quad (32)$$

Then, by taking into consideration that a perfect compensation is achieved, Equations (33) and (34) are modified by adding the current controller response as:

$$L_k\frac{di_{kD}}{dt} = -R_k i_{kD} + k_C(i_{kD}^* - i_{kD}) + k_C\gamma_{kD} - k_\zeta v_{ckD} \quad (33)$$

$$L_k\frac{di_{kQ}}{dt} = -R_k i_{kQ} + k_C(i_{kQ}^* - i_{kQ}) + k_C\gamma_{kQ} - k_\zeta v_{ckQ} \quad (34)$$

In conclusion, including the voltage and current control loops the set of dynamic equation can be represented in the state space by the following twenty two state variables $\Delta\mathbf{x} = [\Delta u_D, \Delta u_Q, \Delta\phi_D, \Delta\phi_Q, \Delta i_{kD}, \Delta i_{kQ}, \Delta\gamma_{kD}, \Delta\gamma_{kQ}, \Delta v_{ckD}, \Delta v_{ckQ}, \Delta V_{kr}, \Delta I_{kco}, \Delta I_{ksc}]^T$, two external inputs $[\Delta P_{WFD}, \Delta Q_{WFQ}]^T$ and four control variables, two for each VSC $[\Delta m_{kD}, \Delta m_{kQ}]^T$. Six new state variables have been added to the state space model obtained in Section III: two representing the states of the voltage controller ϕ_D and ϕ_Q and four more representing the state of the current controller of each VSC γ_{kD} and γ_{kQ} . In order to assess the dynamics and stability of the overall system the eigenvalue analysis is performed in the base-case scenario given in the Appendix.

For this base-case the eigenvalues are computed and presented in Table I. Frequency and damping ratio are also given, as well as the dominant states according to their participation factors [36]. This table shows that all eigenvalues have negative real parts indicating stable operating condition for the base-case scenario. Eigenvalues $\lambda_{1,2}$ and $\lambda_{3,4}$ have the highest frequency oscillation modes and are sensitive to the state variables of the capacitor and filter inductor. Eigenvalues for the DC cables are all overdamped (λ_7 to λ_{10} and $\lambda_{15,16}$). Eigenvalues $\lambda_{11,12}$ and $\lambda_{13,14}$ present low frequency oscillations modes produced by the voltages on the series capacitors. Specifically, the mode corresponding to eigenvalues $\lambda_{13,14}$ present a small damping ratio 0.04. In fact this mode has a negative real part because a damping factor has been included in the control. The modes of eigenvalues $\lambda_{1,2}$ and $\lambda_{3,4}$ are strongly dependent on the voltage and current control loop bandwidths. In a high power VSC control the conventional switching frequency is around 2-3 kHz, and even lower for voltage-balancing algorithms [37]. On the other hand, in order to guarantee a proper response, a sample rate up to 10 times the envisaged bandwidth is used. The usual practice in power electronics control is to select a sampling frequency equal to the switching frequency or higher when over-sampling approaches are taken. In the case of MMC, the effective frequency observed is much higher than the switching frequency, due to the multilevel nature of the converter [38]. Choosing an inner loop 3 times faster than the outer loop [39], the inner current control loop bandwidth has been set at 1888 rad/s (300 Hz) and the outer voltage control loop bandwidth at 683 rad/s (108 Hz). On the other

Table I: Base-case eigenvalue analysis

λ_i	Eigenvalues (rad/s)	Frequency (Hz)	Damping ratio (p.u.)	Dominant states	Participation factors (>0.1)
$\lambda_{1,2}$	-1830±j3822	608	0.43	u_D, i_{1D}, i_{2D}	0.47,0.23,0.23
$\lambda_{3,4}$	-780±j3392	540	0.22	u_Q, i_{1Q}, i_{2Q}	0.47,0.23,0.23
λ_5	-2420			i_{1D}, i_{2D}	0.38,0.38,
λ_6	-2420			i_{1Q}, i_{2Q}	0.37,0.37
λ_7	-1778			I_{1sc}, I_{2sc}	0.33,0.33
λ_8	-1778				
λ_9	-571			I_{1sc}, I_{1c0}, V_{1r}	0.20,0.15,0.13
λ_{10}	-571			I_{2sc}, I_{2c0}, V_{2r}	0.20,0.15,0.13
$\lambda_{11,12}$	-229±j352	56	0.54	$u_{1cD}, u_{2cD},$	0.20,0.20
				u_{1cQ}, u_{2cQ}	0.20,0.20
$\lambda_{13,14}$	-11±j292	47	0.04	$u_{1cD}, u_{2cD},$	0.23,0.23
				u_{1cQ}, u_{2cQ}	0.23,0.23
λ_{15}	-101			I_{1sc}, I_{2sc}	0.33,0.33
λ_{16}	-101				
λ_{17}	-13			γ_{1D}, γ_{2D}	0.27,0.27
λ_{18}	-13			γ_{1Q}, γ_{2Q}	0.23,0.23
$\lambda_{19,20}$	-7±j5	0.75	0.82	γ_{1D}, γ_{2D}	0.25,0.25
				γ_{1Q}, γ_{2Q}	0.25,0.25
λ_{21}	-1.7			ϕ_D	0.95
λ_{22}	-2.4			ϕ_Q	0.95

hand, Figure 8 shows the $\lambda_{1,2}$ and $\lambda_{3,4}$ eigenvalues loci as a function of the WF active power for different values of the AC capacitance, C=0.1, 0.15, 0.2 p.u. This figure shows that while eigenvalues $\lambda_{1,2}$ become more stable, eigenvalues $\lambda_{3,4}$ move toward the unstable side of the plane. Note that for a low capacitance, eigenvalues $\lambda_{3,4}$ can become unstable for high power. It is also worth noting that this instability is due to eigenvalues sensible to the Q component of the voltage and current and hence to the frequency control.
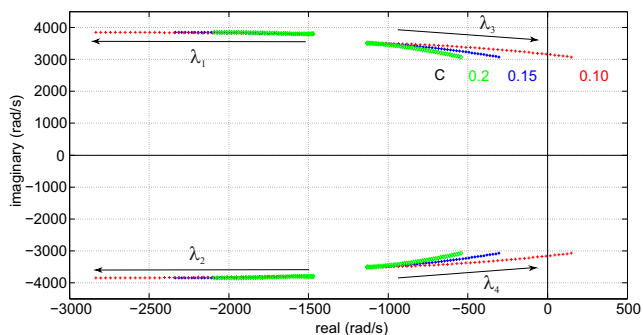
Figure 8: Eigenvalues $\lambda_{1,2}$, $\lambda_{3,4}$ loci as a function of ΔP, C

The control of modern MMC-VSC requires low switching frequency strategies to provide more efficient converter stations [40, 41]. These strategies can lead to the design of voltage and current control loops with low bandwidth and can result in a poor dynamics and low stability margins when power controller blocks are incorporated into the VSC control structure, like droop control techniques. Although the individual voltage and current controller are designed to be stable, their interaction with the slow dynamics of the power controller block (active and reactive droop control and its corresponding secondary controllers) can affect the system stability, resulting in a narrow range of stable operation. The stability of power droop controllers is highly affected by the gain of the droop. This means that frequency error is limited by the control stability. The conventional droop control introduces low frequency dominant modes of operation in comparison with the voltage and the current controllers whose operational modes are more sensitive to

higher frequencies [42]. For this reason, the dynamics of the direct control of voltage and frequency at PCC improves the performance of the conventional droop control. This is possible because the two VSC are connected to the same PCC bus.

VI. SIMULATION RESULTS

The validation of the proposed control system for the voltage and frequency control in an OWF with two parallel VSC has been done by detailed simulation in PSIM. In this section the simulation results are presented and discussed. The simulated system consists of a 800 MW OWF connected to the grid through two 245 kV VSC HVDC links. The main system parameters are given in the Appendix. The OWF has been modelled by aggregation of two equivalent wind turbines (one for each AC line). For each WT the front-end converter has been completely modelled, including the current control loops and using as inputs P_{WF} and Q_{WF}. Simulation results show the system response to various scenarios. For the first case, starting at P_{WF} =250 MW and Q_{WF} =0, the OWF active power is suddenly increased up to 500 MW at t=1 s., while at t=3 s reactive power is increased from 0 to 25 MVAr. Figure 9a shows that the OWF active power step produces a transient in the voltage D-component, i.e. voltage magnitude, while the reactive power step hardly affects the voltage magnitude. On the other hand, a small disturbance can be seen in the voltage Q-component, i.e. voltage frequency, under both input steps. To be more precise, frequency response is also presented in Figure 9a. Nevertheless, it has to be pointed that for the proposed frequency control scheme, the frequency measurement is not needed, so the frequency signal shown in this section has been obtained by means of a PLL only for displaying purposes. The transients are quickly compensated in both cases, which demonstrate the capability of the proposed VFC. This figure also demonstrates that voltage magnitude and frequency responses are practically decoupled: the active power step mainly affects the voltage magnitude, while the reactive power mainly affects the frequency.
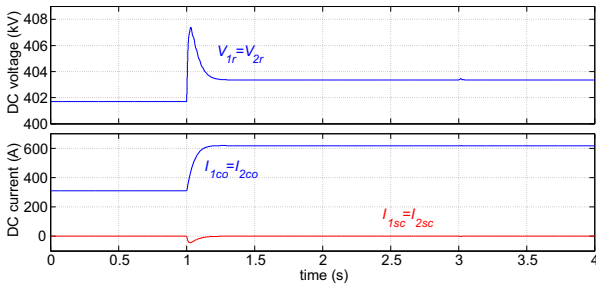
On the other hand, Figure 9b shows that the incoming OWF active and reactive power is divided exactly by two be-
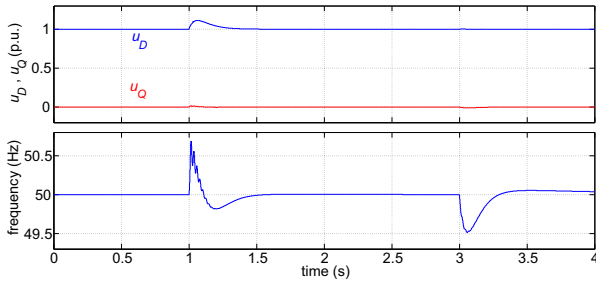
(a) Voltage dq components and voltage frequency
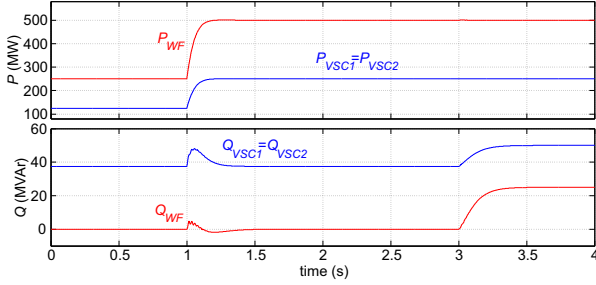
(b) Active and reactive power at each converter and from the wind farm

(c) Rectifier DC voltage and DC cable current

Figure 9: Active and reactive power step changes

tween both converters, meaning that both of them participate in the same proportion in the voltage and frequency control. Note that for the reactive power response, the difference between the incoming reactive power from the wind farm and the reactive power taken by both converters is the reactive power at the PCC capacitance. Finally, Figure 9c also shows the voltage and current at the DC side of each converter. These results show the DC voltage and current increasing as a result of the power increasing and also the cable screen current.

Moreover, to demonstrate the operational flexibility of participation factors, a second simulation has been performed where the second VSC operates under constant active and reactive power mode, set at 125 MW and 37.5 MVAr, while the first VSC assumes the voltage and frequency control. Figure 10 shows the system response. The inputs are the same as the previous case. When the OWF active power increases and so later the reactive power, the second VSC continues evacuating 125 MW and 37.5 MVAr, while the first converter assumes the control, balancing active and reactive power at the bus.
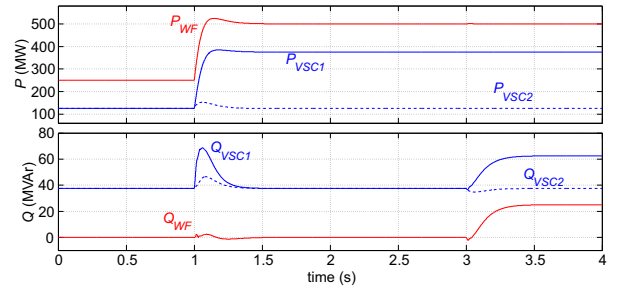

Figure 10: Active and reactive power at each converter and from the wind farm

Finally, the response to a system fault has been obtained. In this simulation the system is initially operating at full load in steady state and at t=0.2s a fault is applied in one of the lines interconnecting the offshore substation and the VSCs station (see Figure 1) during 300 ms. The fault produces a voltage sag to nearly zero, as the VFC cannot control the voltage magnitude during the fault. Figure 11 shows the voltage magnitude at the capacitor terminals as well as the instantaneous voltage and the frequency in one phase. During the fault voltage drops to nearly zero because the voltage controller reaches saturation due to the low voltage condition at the AC terminals. Nevertheless, frequency control is still possible based on the residual voltage at the capacitors, as shown in Figure 11.
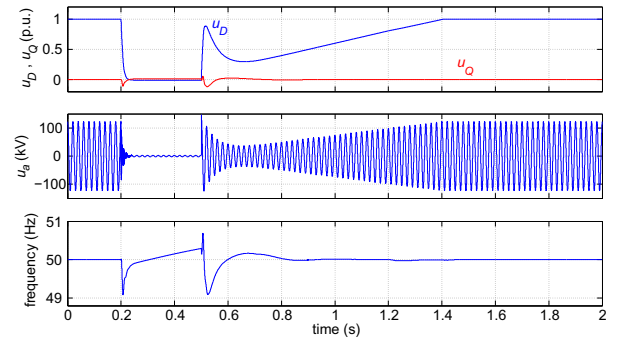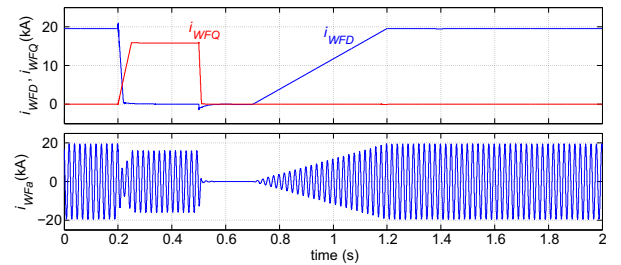

Figure 11: Voltage and frequency during the fault

Figure 12: Wind farm DQ and instantaneous current during the fault

Finally, at t=0.5s the fault is cleared. Figure 11 shows that voltage is quickly restored based on the fast response of the current control loop and frequency is well regulated even during the transient. Of course, the response during the fault

and post-fault is very dependent on the so-called low voltage ride through (LVRT) response of the wind turbines. The OWF-LVRT response is given in Figure 12. Active current is reduced to zero during the fault while injecting maximum reactive current, as it is usually demanded in many grid codes [43]. Moreover, after the fault is cleared, the voltage is increased gradually in order to avoid overvoltage and also transformer inrush, while WTs do not start injecting current until a certain level of voltage is reached. This figure also shows the OWF instantaneous current in one phase. Figure
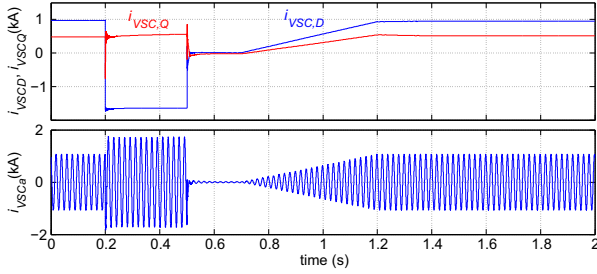

Figure 13: VSC DQ and instantaneous current during the fault

13 shows the VSCs current response. As it has been stated, during the fault the voltage controller reaches saturation. Maximum current is then injected to the bus but it is not enough to control the voltage. Nevertheless, on the other channel, frequency control is still possible because it is based on the vector orientation, which does not depend on the voltage vector magnitude. When the fault is cleared, the strategy implemented consists of increasing voltage gradually in order to avoid overvoltage. As a result, current is increased also gradually.

VII. CONCLUSIONS

This paper has presented a voltage and frequency control system for the parallel operation of two VSC-HVDC links connected to an offshore wind farm. In the paper, the system state-space model was first obtained and then the principles for the voltage and frequency control were established. The proposed control system allows the decoupled control of the voltage and frequency in the OWF, while allowing the parallelization of both VSCs by setting current commands to each converter in order to maintain constant voltage and frequency within the OWF grid. Therefore, the parallel operation of the two converters is inherent to the proposed control method. Moreover, it is possible to establish a constant power operation mode in one VSC, while the other keeps the responsibility of controlling voltage and frequency. The proposed controller stability was studied using the state-space model, demonstrating the stability of the proposed VFC through eigenvalue analysis. Furthermore, a detailed switching-model developed in PSIM has also been used to validate the proposed control system. This validation demonstrates the performance of the proposed control system for controlling voltage and frequency during normal operation and under a fault disturbance.

APPENDIX

Parameters AC side [7]

- Parameters AC: $U_{ac,B}$=245 kV, S_{base}=500 MVA, ω_0=100π rad/s
- Parameters DC: $U_{dc,b}$=400 kV, P_{base}=500 MW
- VSC transformers (T1 and T2): 500 MVA, 245/150 kV, short circuit impedance 10% (X/R=10)
- Wind farm step-up transformers (T3 and T4): 450 MVA, 150/33 kV, short circuit impedance 5% (X/R=10)
- High frequency filter capacitance: 37.5 MVAr (245 kV)
- AC export Cables: length=10 km, L=0.2526 mH/Km, R=0.0843 Ω/km, C=0.1837 μF/km, G=0.041 μS/km

VSC Converters

- Arm reactor 15% (57.32 mH), Arm resistance 0.9% (1.08 Ω), number of submodules per arm: Narm=400, cell voltage V_{cell}=400 kV/400=1 kV, energy storage per submodule E_s=30 kJ/MVA, Cell Capacitance: $C_{cell} = 2S_B E_S/6N_{arm}v_{cell}^2$=25mF, Arm Capacitance: $C_{arm} = C_{cell}/N_{arm} = 62.5$ μF (2.36 p.u)

Parameters DC side [30, 7]

- DC cables $\pm$200 kV, 200 km
- Parameters DC cable: Core resistance R_{co}=0.011 mΩ/km, Screen resistance R_{sc}=0.22 mΩ/km, Core inductance L_{co}=2.6 mH/km, Screen inductance L_{sc}=2.5 mH/km, Core-screen mutual inductance M_{cs}=2.5 mH/km, Core to ground conductance G_{cb}=0.055 μS/km, Core to ground capacitance C_{cb}=0.2185 μF/km,

Table II shows the parameters of the voltage and frequency regulators as well as the damping factor chosen to ensure the stability of the system.

Table II: Current and voltage controller parameters

Current Controller PI$_C$
K_c=0.62 p.u. (74.4 V/A)
T_c=100 ms
Voltage Controller PI$_V$
K_v=0.64 p.u. (0.0053 A/V)
T_v=500 ms
Damping factor
K_ζ=25 p.u.

REFERENCES

[1] P. Bresesti, W. L. Kling, R. L. Hendriks, and R. Vailati, "Hvdc connection of offshore wind farms to the transmission system," *Energy Conversion, IEEE Transactions on*, vol. 22, no. 1, pp. 37–43, 2007.

[2] H.Li and Z. Chen, "Overview of different wind generator systems and their comparison," *IET Renewable Power Generation*, vol. 2, pp. 123–138, 2008.

[3] D. V. Hertem, O. Gomis-Bellmunt, and J. Liang, *HVDC Grids: For Offshore and the Supergrid of the Future.* Wiley-IEEE Press, 2016.

[4] A. Kirakosyan, M. S. E. Moursi, and V. Khadkikar, "Fault ride through and grid support topology for the VSC-HVDC connected offshore wind farms," *IEEE Transactions on Power Delivery*, vol. 32, no. 3, pp. 1592–1604, June 2017.

[5] A. Moawwad, M. S. E. Moursi, and W. Xiao, "Advanced fault ride-through management scheme for VSC-HVDC connecting offshore wind farms," *IEEE Transactions on Power Systems*, vol. 31, no. 6, pp. 4923–4934, Nov 2016.

[6] W. Leterme, P. Tielens, S. D. Boeck, and D. V. Hertem, "Overview of grounding and configuration options for meshed hvdc grids," *IEEE Transactions on Power Delivery*, vol. 29, no. 6, pp. 2467–2475, 2014.

[7] "CIGRÉ Working Groups B4-58 (Devices for load flow control and methodologies for direct voltage control in a meshed HVDC grid) and B4-57 (Guide for the development of models for HVDC converters in a HVDC grid). The CIGRÉ B4 DC grid test system," *International Council for Large Electric Systems (CIGRÉ)*, 2013.

[8] A. Yazdani and R. Iravani, *Voltage-Sourced Converters in Power Systems: Modelling, Control, and Applications.* John Wiley & Sons, 2010.

[9] "CIGRÉ Working group B4-55, Technical Brochure 619, HVDC connection of offshore wind power plants," *International Council for Large Electric Systems (CIGRÉ)*, 2015.

[10] A. Raza and O. Gomis, "Multi infeed control of VSC HVDC transmission system for offshore wind power plant integration," in *13th International Workshop on Large Scale Integration of Wind Power into Power Systems as well as on Transmission Networks for Offshore Wind Plants, Berlin*, 2014.

[11] S. D'Arco, J. Suul, and O. Fosso, "Control system tuning and stability analysis of virtual synchronous machines," in *Energy Conversion Congress and Exposition (ECCE), 2013 IEEE, Denver (CO), USA*, Sept 2013, pp. 2664–2671.

[12] M. Guan, W. Pan, J. Zhang, Q. Hao, J. Cheng, and X. Zheng, "Synchronous generator emulation control strategy for voltage source converter (vsc) stations," *IEEE Transactions on Power Systems*, vol. 30, no. 6, pp. 3093 – 3101, 2015.

[13] S. D'Arco and J. A. Suul, "Equivalence of virtual synchronous machines and frequency-droops for converter-based microgrids," *IEEE Transactions on Smart Grid*, vol. 5, no. 1, pp. 394 – 395, 2014.

[14] L. Zhang, "Modeling and control of VSC-HVDC links connected to weak ac systems," in *PhD*, 2014.

[15] V. F. Lescale, O. R. Holmberg, P., and Y. J. Hafner, "Parallelling offshore wind farm hvdc ties on offshore side," in *International Council for Large Electric Systems (CIGRÉ) Session Paris, paper C1-107*, 2012.

[16] K. Schönleber, S. Ratés-Palau, and O. Gomis-Bellmunt, "Analysis of reactive power strategies in hvdc-connected wind power plant clusters," *Wind Energy*, vol. 20, no. 12, pp. 1971–1982, 2017. [Online]. Available: http://dx.doi.org/10.1002/we.2134

[17] K. Schönleber, C. Collados, R. T. Pinto, S. Ratés-Palau, and O. Gomis-Bellmunt, "Optimization-based reactive power control in hvdc-connected wind power plants," *Renewable Energy*, vol. 109, no. Supplement C, pp. 500 – 509, 2017.

[18] S. Cole, J. Beerten, , and R. Belmans, "Generalized dynamic VSC MTDC model for power system stability studies," *IEEE Transactions on Power Systems*, vol. 25, no. 3, pp. 1655–1662, 2010.

[19] A. Yazdani and R. Iravani, "A unified dynamic model and control for the voltage-sourced converter under unbalanced grid conditions," *IEEE Transactions on Power delivery*, vol. 21, no. 3, pp. 1620–1629, 2006.

[20] A. Xu, L., B. R., and P. Cartwright, "VSC transmission operating under unbalanced ac conditions-analysis and control design," *IEEE Transactions on Power delivery*.

[21] A. Beddard, M. Barnes, and R. Preece, "Comparison of detailed modeling techniques for MMC employed on VSC-HVDC schemes," *IEEE Transactions on Power Delivery*, vol. 30, no. 2, pp. 579–589, April 2015.

[22] C. Du and E. Agneholm, "Investigation of frequency/ac voltage control for inverter station of VSC-HVDC," in *IECON 2006-32nd Annual Conference on IEEE Industrial Electronics. IEEE*, 2006, pp. 1810–1815.

[23] H. Saad *et al.*, "Dynamic averaged and simplified models for MMC-based HVDC transmission systems," *IEEE Transactions on Power Delivery*, vol. 28, no. 3, pp. 1723–1730, July 2013.

[24] H. Saad, X. Guillaud, J. Mahseredjian, S. Dennetière, and S. Nguefeu, "MMC capacitor voltage decoupling and balancing controls," *IEEE Transactions on Power Delivery*, vol. 30, no. 2, pp. 704–712, 2015.

[25] M. Vasiladiotis, N. Cherix, and A. Rufer, "Accurate capacitor voltage ripple estimation and current control considerations for grid-connected modular multilevel converters," *IEEE Transactions on Power Electronics*, vol. 29, no. 9, pp. 4568–4579, 2014.

[26] R. Darus *et al.*, "A modified voltage balancing algorithm for the modular multilevel converter: Evaluation for staircase and phase-disposition PWM," *IEEE Transactions on Power Electronics*, vol. 30, no. 8, pp. 4119–4127, 2015.

[27] J. W. Moon, C. S. Kim, J. W. Park, D. W. Kang, and J. M. Kim, "Circulating current control in MMC under the unbalanced voltage," *IEEE Transactions on Power Delivery*, vol. 28, no. 3, pp. 1952–1959, 2013.

[28] D. Jovcic and A. Jamshidifar, "Phasor model of modular multilevel converter with circulating current suppression control," *IEEE Transactions on Power Delivery*, vol. 30, no. 4, pp. 1889–1897, 2015.

[29] S. Akkari, J. Dai, M. Petit, P. Rault, and X. Guillaud, "Small-signal modelling for in-depth modal analysis of an mtdc system," in *Electrical Power and Energy Conference (EPEC)*, 2015.

[30] P. Rault, "Dynamic modeling and control of multi-terminal HVDC grids," in *PhD*, 2014.

[31] J. Aliakbar and D. Jovcic, "Small-signal dynamic dq model of modular multilevel converter for system studies," *Power Delivery, Transactions on*, vol. 31, no. 1, pp. 191–199, 2016.

[32] D. Jovcic and K. Ahmed, *High voltage direct current transmission: converters, systems and DC grids*. John Wiley & Sons, 2015.

[33] "CIGRÉ Working group B4-57, Technical Brochure 604, Guide for the Development of Models for HVDC Converters in a HVDC Grid," *International Council for Large Electric Systems (CIGRÉ)*, 2014.

[34] M. B. Delghavi and A. Yazdani, "A control strategy for islanded operation of a distributed resource (dr) unit," in *2009 IEEE Power Energy Society General Meeting*, July 2009, pp. 1–8.

[35] N. Chaudhuri, A. Yazdani, B. Chaudhuri, and R. Majumder, *Multi-terminal Direct-current Grids: Modeling, Analysis, and Control*. John Wiley & Sons, 2014.

[36] P. Kundur, N. Balu, and M. Lauby, *Power system stability and control*, ser. EPRI power system engineering series. McGraw-Hill, 1994.

[37] Q. Tu, Z. Xu, and L. Xu, "Reduced switching-frequency modulation and circulating current suppression for modular multilevel converters," in *Transmission and Distribution Conference and Exposition (T D), 2012 IEEE PES*, May 2012.

[38] K. Sharifabadi, L. Harnefors, H.-P. Nee, S. Norrga, and R. Teodorescu, *Introduction to Modular Multilevel Converters*. John Wiley & Sons, 2016, pp. 7–59.

[39] S. K. Lahiri, *Multivariable Predictive Control: Applications in Industry*. John Wiley & Sons, 2017.

[40] A. Hassanpoor, S. Norrga, and A. Nami, "Loss evaluation for modular multilevel converters with different switching strategies," in *9th International Conference on Power Electronics and ECCE Asia*.

[41] Q. Tu, Z. Xu, and L. Xu, "Reduced switching-frequency modulation and circulating current suppression for modular multilevel converters," *IEEE Transactions on Power Delivery*, vol. 26, no. 3, pp. 2009–2017, July 2011.

[42] N. Pogaku, M. Prodanovic, and T. C. Green, "Modeling, analysis and testing of autonomous operation of an inverter-based microgrid," *IEEE Transactions on Power Electronics*, vol. 22, no. 2, pp. 613–625, 2007.

[43] E. N. of Transmission System Operators for Electricity, "Requirements for grid connection applicable to all generators," March 2013.